RSC Advances

ROYAL SOCIETY OF CHEMISTRY

www.rsc.org/advances

RSC Advances

ARTICLE

Interlayer coupling of direct van der Waals epitaxial MoS_2/ graphene heterostructure

Received 00th January 20xx,
Accepted 00th January 20xx

DOI: 10.1039/x0xx00000x

www.rsc.org/

Wen Wan,[a] Xiaodan Li,[a] Xiuting Li,[a] Binbin Xu,[b] Linjie Zhan,[a] Zhijuan Zhao,[a] Peichao Zhang,[a] S.Q. Wu,[a] Zi-zhong Zhu,[a,c] Han Huang,[d] Yinghui Zhou*[a] and Weiwei Cai*[a]

Many efforts have been undertaken towards the synthesis of the vertically stacked two-dimensional (2D) crystals due to their unique electronic and optical properties. Here, we present a direct molecular beam epitaxy (MBE) growth of MoS_2/graphene heterostructure by a strict epitaxial mechanism. By combining Raman, photoluminescence, transmission electron microscopy characterizations and first-principles calculations, we find that there exists a strain effect and strong interlayer coupling between MoS_2 and graphene resulting from the intrinsic crystal lattice mismatch, which could generate a potential metallic behavior of the heterostructure. The direct epitaxial technique applied here enables us to investigate the growth mechanisms and interlaminar interaction of 2D heterostructures without sample handling and transfer, and offers a new approach to synthesize multilayer electronic and photonic devices.

Introduction

Two-dimensional (2D) materials, such as semi-conductive transition metal dichalcogenides (TMDCs), [1-3] phosphorene, [4] and insulative hexagonal boron nitride (*h*-BN), [5] have attracted increasing interest for the supplement of graphene (Gr) with zero-gap feature. Additionally, owing to the combination of two or more of these layered 2D materials, lots of new and promising electronic and optical properties as well as good mechanical flexibility can be achieved. [6, 7, 8]

Among the class of 2D materials, Gr and monolayer MoS_2 have shown many advantages and can complement each other. The former has extremely high carrier mobility, but its gapless and low optical absorption in the visible light range have limited the application in the future; the latter has a band gap of 1.9 eV and shows high optical absorption. Their versatile heterostructures have been developed in photoelectronic devices, [9] logic transistors [10] and nonvolatile memories. [11] Additionally, some new physical phenomena resulting from the strong interaction in such heterostructures have also been theoretically described. [8, 12, 13] Mechanical exfoliation followed by transfer is the most common method to prepare vertically stacked MoS_2/Gr heterostructures nowadays. [7-11] But its drawbacks are obvious, for instance, the limited flake sizes, the uncontrollable layer number, and impurities embedded in the interface. Moreover, barely lattice orientation consistency between the layered materials can be preserved, which would significantly affect the properties of the heterostructures.

In order to settle this issue, some ingenious studies have conducted to grow MoS_2 directly on freestanding chemical vapor deposition Gr (CVD-Gr) [14] or the Gr transferred on SiO_2/Si, [15, 16] however, those methods do not completely solve all the difficulties. The transfer of Gr from its substrate is more likely to cause defects, and would also introduce stubborn impurities such as PMMA before the next step of MoS_2 growth. To avoid the issues of polymer residues, utilizing epitaxial Gr on 6H-SiC as the template for directly growth of MoS_2 has provided technological advantages, [17] but challenges still exist in the utilization of epitaxial Gr (uniform thickness over large areas, steps in the SiC surface). Other possibilities of direct growth of MoS_2 over a Gr-covered Cu foil [18] or as-grown Gr on Cu (111)/sapphire [16] have been studied, which are significant advances in the pursuit of van der Waals solids. However, the temperature employed in the CVD growth of MoS_2 is so high that the Cu substrate reacts with the sulfur in the chamber, making the Cu surface blackened or even etched completely. Therefore, Pt foil, a comparatively inert substrate covered with CVD-Gr, has first been used as the template for the growth of MoS_2 in our work. Scanning electron microscope (SEM), Raman spectroscopy, photoluminescence (PL), transmission electron microscopy (TEM), X-ray photoelectron spectroscopy (XPS), and density functional theory (DFT) calculations have been utilized to investigate the epitaxial properties on the prepared

[a] Department of Physics, Xiamen University, Xiamen, Fujian 361005, China. E-mail: yhzhou@xmu.edu.cn, wwcai@xmu.edu.cn.
[b] School of Chemistry and Chemical Engineering, Xiamen University, Xiamen, Fujian 361005, China
[c] Fujian Provincial Key Laboratory of Theoretical and Computational Chemistry, Xiamen, Fujian 361005, China
[d] Institute of Super-microstructure and Ultrafast Process in Advanced Materials, School of Physics and Electronics, Central South University, Changsha, Hunan 410083, China

†Electronic Supplementary Information (ESI) available. See DOI: 10.1039/x0xx00000x

MoS_2/Gr heterostructure. We found that the existence of effective interlayer coupling and considerable strain between the strictly epitaxial MoS_2 crystals and the Gr substrate due to the intrinsic crystal lattice mismatch of the two layered materials could have a significant effect on the structural and electronic properties of MoS_2/Gr heterostructure.

Experimental and computational methods

Sample Preparation

CVD-Gr synthesis. Single layer Gr was synthesized on a 0.25 mm thick Pt foil (Alfa Aesar, stock #012058, purity 99.997wt. %) in a quartz tube furnace. After pumping down to 5.0×10^{-1} Pa, 10sccm hydrogen gas was introduced into the growth chamber with a total pressure of ~15 Pa and the chamber was heated to and kept at 1050 ℃ for 20 min to initiate Pt grain growth and remove residual oxide on the surface. Subsequently, 5 sccm methane gas was introduced with a total pressure of ~25Pa to the growth chamber for Gr synthesis and maintained for 20 min. After the synthesis, the introduction of hydrogen and methane was stopped and the chamber was first cooled down to 600 ℃ at a slow rate of ~10 ℃/min and then quickly cooled down to room temperature.

MoS_2 synthesis. CVD-Gr on 0.25 mm thick Pt foil used as the substrate was placed into the home-built MBE chamber and faced downwards to two PBN crucibles, which respectively contain MoO_3 (stock #10812, purity 99.998%) and S powder (stock #43766, purity 99.95%), both from Alfa Aesar. First, the substrate was annealed to 600 ℃ with a vacuum condition of better than 5.0×10^{-4} Pa to clean the Gr surface and reduce the oxygen species which may exists. Then, MoO_3 and S powder were thermally vaporized to synthesize MoS_2 on the CVD-Gr surface for 30-60 min. The substrate was kept at 600 ℃ under sulfur atmosphere for 30 min before cooling down to room temperature. During the process of MoS_2 growth, the pressure was better than 6.0×10^{-3} Pa.

Electrochemical bubbling method for transfer of MoS_2/Gr from Pt foil. Firstly, the MoS_2/Gr surface was covered with a Poly [methylmethacrylate] (PMMA) film by spin coating. Then the sample was immersed in an aqueous solution of 1 M NaOH for an electrochemical delamination. The PMMA/MoS_2/Gr/Pt foil sample and a bare Pt foil were utilized as a cathode and an anode, respectively. The bubbling transfer was performed at a constant current of 0.2A (corresponding electrolytic voltage of 3-5V) for 1-5min. After peeling off the PMMA/MoS_2/Gr film from Pt foil, it was rinsed with deionized water to remove the residual NaOH solution and then transferred to arbitrary substrates. Finally, PMMA was removed by dipping the film into acetone solution.

Characterizations

The surface morphology of MoS_2/Gr/Pt was characterized by scanning electron microscope (Zeiss Sigma). Raman spectra and photoluminescence were measured using a micro Raman spectrometer (Alpha 300, WITec) with a 488nm laser. XPS measurements were performed to determine the chemical composition of the as-grown films with monochromatic AlKα radiation (1486.6eV) using a PHI Quantum 2000 system (40W, 200μm spot size, 0.1eV resolution). A field-emission transmission electron microscope (JEM-2100, operated at 200keV) was used for ultra-high-resolution imaging of the MoS_2/Gr along with selected area electron diffraction (SAED) pattern.

Computational methods

Our calculations were carried out using the projector augmented wave (PAW) [19] method within the density functional theory (DFT) as implemented in the Vienna *ab* initio simulation package (VASP). [20, 21] Electronic exchange-correlations functional was treated within the local density approximation (LDA). [22, 23] Wave functions are expanded in plane waves up to a kinetic energy cut-off of 420eV. Brillouin-zone integrations are approximated by using special k-point sampling of Monkhorst-Pack scheme with a gamma centered 6×6×3 grid. Atomic coordinates were fully relaxed until the Hellmann-Feynman force on each atom was smaller than 0.01 eV $Å^{-1}$.

Results and discussion

Fig. 1 shows a schematic diagram of the MBE growth of MoS_2 on the Gr/Pt substrate as well as the subsequent transfer of MoS_2/Gr heterostructure to SiO_2 or TEM grids. The commonly used etching-based transfer method for Cu and Ni substrates is not suitable for the transfer of the MoS_2/Gr layers grown on Pt foil because Pt is an expensive and chemically inert material. Recently, a bubbling-based electrochemical delamination technique was successfully used to transfer the *h*-BN layer grown on Pt foil onto SiO_2/Si substrates. [5] Using this method, the MoS_2/Gr heterostructure can be transferred to arbitrary substrates, and the Pt foil can be recycled since it is not

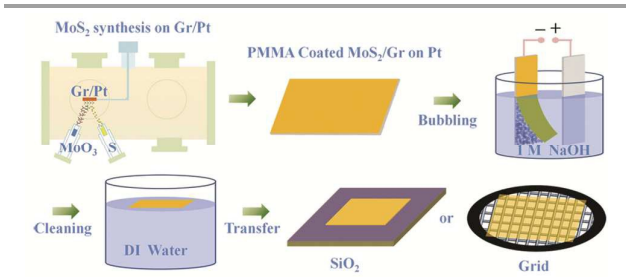

Fig. 1 Schematic flow diagram of the MBE growth of MoS_2 film on Gr/Pt and the subsequent transfer process of MoS_2/Gr film to SiO_2 or TEM grids.

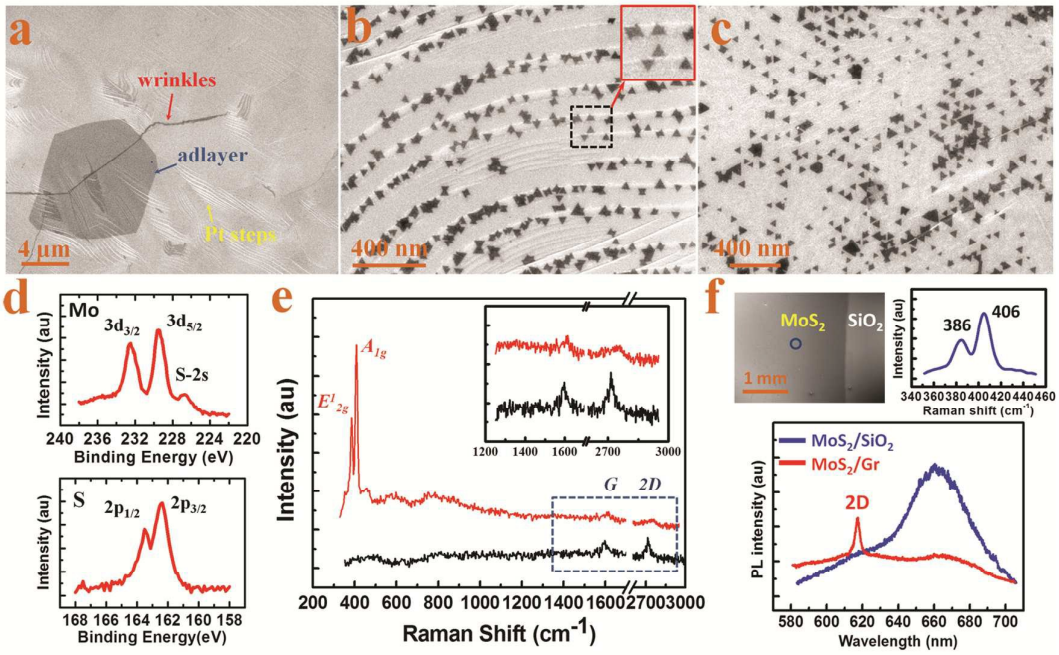

Fig. 2 (a-c) SEM images of MoS_2 crystallites grown on Gr/Pt. (a) As-grown CVD-Gr on Pt foil; (b) MoS_2 crystallites on the ripples of Gr that induced by Pt steps (the enlarged crystallites in black dotted frame are shown in the upper-right corner of (b)); (c) MoS_2 crystals grown on Gr/Pt with few ripple. (d) Mo 3d and S2p XPS spectra from the as-grown MoS_2 on Gr/Pt. (e) Raman spectra of Gr/Pt before (black) and after (red) the growth of MoS_2. The enlarged G and 2D bands are illustrated in the upper-right corner of (e). (f) (Top panel) SEM image and Raman spectrum of a large scale monolayer MoS_2 film grown on SiO_2. (Bottom panel) Photoluminescence spectra of MoS_2 grown on Gr (red) and SiO_2 (blue), respectively. The peak of 2D indicates the 2D band of Gr. The Raman and photoluminescence spectra of MoS_2 on SiO_2 are taken in the blue circle on the SEM image.

consumed during the process. The preparation and transfer of MoS_2/Gr heterostructure have been described in detail in the Experimental and computational methods section.

The characteristics of MoS_2 crystallites grown on Gr/Pt are shown in Fig. 2. The preparation of Gr on a Pt foil with CVD method is similar to the previous works [24-26]. Gr wrinkles and adlayer can be clearly seen, as commonly appear in CVD-Gr on Cu foil. [27] The steps of Pt are also visible underneath the Gr. A good contrast is shown between the grown MoS_2 flakes and the Gr/Pt substrate in the SEM images, as shown in Figure 2b. The MoS_2 flakes appear as equilateral triangles in uniform dark contrast (as illustrated in the upper-right corner of Fig. 2b), which indicates a good crystallinity as previous reports on single layer MoS_2 on Gr by CVD method. [14, 16] It is known that the weak van der Waals forces and the absence of dangling bonds between layers can also provide a route for the crystal to yield a commensurate growth between highly mismatched materials through van der Waals epitaxy. The relatively large lattice mismatch between MoS_2 and Gr (±28%) is expected to be relaxed through the weak van der Waals force. [18] Additionally, we find that most MoS_2 crystals preferentially nucleate along the Pt steps underneath Gr. The more likely reason lies in the ripples of Gr that caused by the fast cooling in the first step of CVD-Gr preparation on Pt substrate. Such ripples can largely release the strain resulting from large lattice mismatch between MoS_2 and Gr during the growth process. For comparison, we adjusted the cooling rate of Pt annealing in a slower speed to restrain the generation of Gr ripples. The MoS_2 flakes grown on Gr with few ripples exhibit a uniform distribution as shown in Fig. 2c, which indicates that the strain in Gr would affect the nucleation and growth of MoS_2.

The chemical composition of the as-grown MoS_2 on CVD-Gr is determined by X-ray photoelectron spectroscopy without removing the underlying Pt foil, as shown in Fig. 2d. The two peaks of Mo 3d orbit are located at 229.5 and 232.5 eV (corresponding to the doublet of Mo $3d_{5/2}$ and Mo $3d_{3/2}$), and the sulfur 2s peak is also showed at 226.6 eV. Additionally, the two peaks at 163.5 eV and 162.4 eV are corresponding to the S $2p_{1/2}$ and S $2p_{3/2}$ orbital. They are well consistent with the previously reported values, [15] and confirm the expected charge states of 2- for S and 4+ for Mo in MoS_2 crystals.

The Raman spectrum of the pristine Gr collected before MoS_2 growth (black in Fig. 2e) shows a high intensity of 2D bands (locating at 2715 cm^{-1}) with respect to the G band (locating at 1598 cm^{-1}) and no D band, proving the high quality of the CVD-grown monolayer Gr. After the MBE growth of MoS_2, both G and 2D bands of the Gr underneath MoS_2 domains (red in Fig. 2e) upshift. The 2D band is upshifted by 18 cm^{-1} (locating at 2733 cm^{-1}), and its intensity is suppressed by MoS_2 as well. There is still no presence of D band after MoS_2

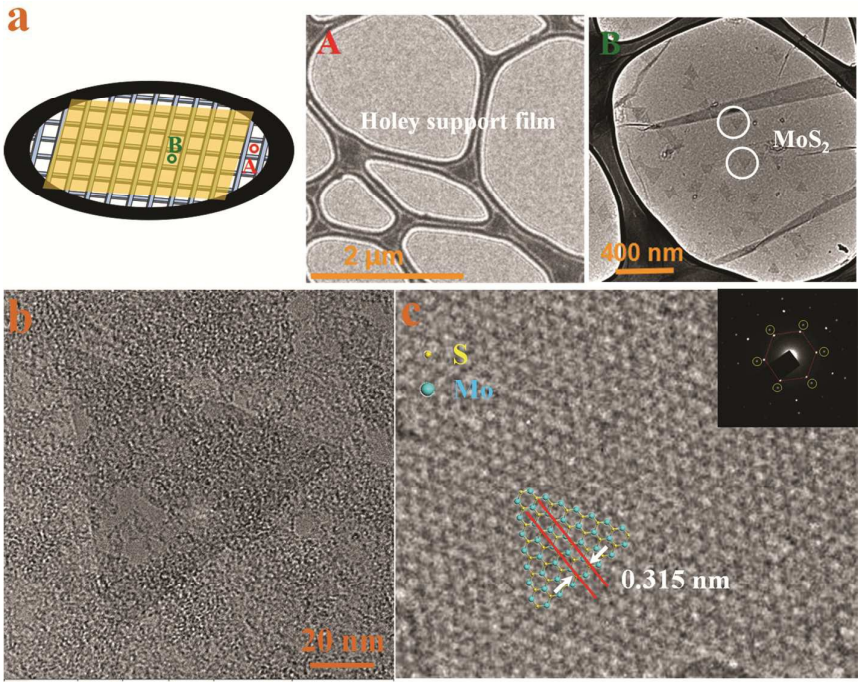

Fig. 3 (a) MoS_2/Gr heterostructure transferred on the holey support film of TEM grids. The pictures A (bare holey support film) and B (with transferred MoS_2/Gr heterostructure) are taken from the corresponding areas marked on the TEM grid. (b) TEM image of a single triangular MoS_2 monocrystal. (c) High resolution TEM image of MoS_2 and selected-area electron diffraction (SAED) in (b), superimposed with a schematic top view on the atomic structure of MoS_2 showing a lattice constant of 0.315 nm.

growth, suggesting that the Gr layer maintains high quality during the MoS_2 MBE process. The upshift of Raman 2D band could be due to the temperature, charge transfer, and strain. [16] In our experiment, the factor of temperature can be ignored, because the measurements were taken at room temperature with a relative low laser power. It is known that the 2D-band shifts up- and downward corresponding to hole and electron doping, respectively. And the I_{2D}/I_G ratio is sensitive to the carrier doping and decreases with doping level increasing. Thus, we suppose that there could be charge transfer between the MoS_2/Gr heterostructure. Additionally, the upshift of the 2D band is also presented in a recent work about mechanically stacked heterostructures, which is explained by the interlayer coupling between Gr and MoS_2. [28] What's more, since MoS_2 and Gr have positive and negative thermal expansion coefficients (TEPs) (= 1.9×10^{-6} K^{-1} for MoS_2 and ~ -8×10^{-6} K^{-1} for Gr, respectively), [29, 30] it is likely that the MoS_2 domains formed at high temperature (typically 650–700 °C) lead to a compressive strain in the Gr after cooling down to room temperature. The mechanical strain in Gr can be calculated from the Raman 2D band shift, which shows a value of 0.3% by a 2D-band position shift of 20 cm^{-1}. [16] So, we suppose that the charge transfer between Gr and MoS_2, the effective interlayer coupling, and strain effect would all contribute to the observed upshift of the Raman G and 2D bands of the Gr.

To further confirm the interfacial charge transfer between Gr and MoS_2, we measured the photoluminescence (PL) of MoS_2/Gr heterostructure transferred on SiO_2, as shown in Fig. 2f. Compared with the monolayer MoS_2 film directly grown on SiO_2, a strong PL quenching (>85%) is observed in the MoS_2/Gr sample. Such PL quenching is also much larger than the MoS_2/Gr heterostructure that MoS_2 transferred on Gr/SiO_2 which shows only 6% decrease, as recently reported by Ago *et al*. [16] This proves a strong electronic interaction and interlayer coupling in our directly epitaxial MoS_2/Gr heterostructure.

The stochastic measurement on CVD-Gr after MoS_2 growth shows two additional Raman peaks; the A_{1g} and $E_{2g}{}^1$ peak, associated with out-of-plane and in-plane vibration, respectively (red spectrum in Fig. 2e). The $E_{2g}{}^1$ and A_{1g} Raman active modes are very sensitive to the alterations of interlayer coupling in different thickness of MoS_2 (the frequency of the former decreases and that of the latter increases with the thickness increase). Thus, the wave number difference in the Raman spectrum of the two modes can also provide convenient and reliable means for determining the layer thickness of MoS_2. The frequency difference between the $E_{2g}{}^1$ and A_{1g} modes is about 20, 22, and 25 cm^{-1} for single layer, bilayer, and bulk MoS_2, respectively. [15, 17, 31] The average separation between the two peaks in our measurements is about 22.5 cm^{-1}, as if the growth of multilayer MoS_2. However, it should be noted that in our case some of the triangular MoS_2 flakes gather together and overlap, which can be seen in Fig. 2c. Additionally, the separation between the two peaks can also be altered by strain, as reported by Wang *et al*. [32] They

confirmed an obvious red-shift occurs to E_{2g}^1 mode with increasing uniaxial tensile strain, while the frequencies of A_{1g} mode kept unchanged, thus resulting in a larger separation. Therefore, we judge that the triangular MoS_2 domains grown on Gr are monocrystals with single layer. The MoS_2 crystallites will be further determined by TEM characterization.

The copper grids we used for TEM characterization all have holey support films on them, as it can well avoid the MoS_2/Gr heterostructures breakage. From the TEM image in Fig. 3a, lots of triangular MoS_2 domains on Gr can be clearly observed. The enlarged TEM image of a single MoS_2 triangular domain is shown in Fig. 3b. Although there is some PMMA residue that we have used for transfer on the surface, it makes no difference to the properties of heterostructures. Fig. 3c shows

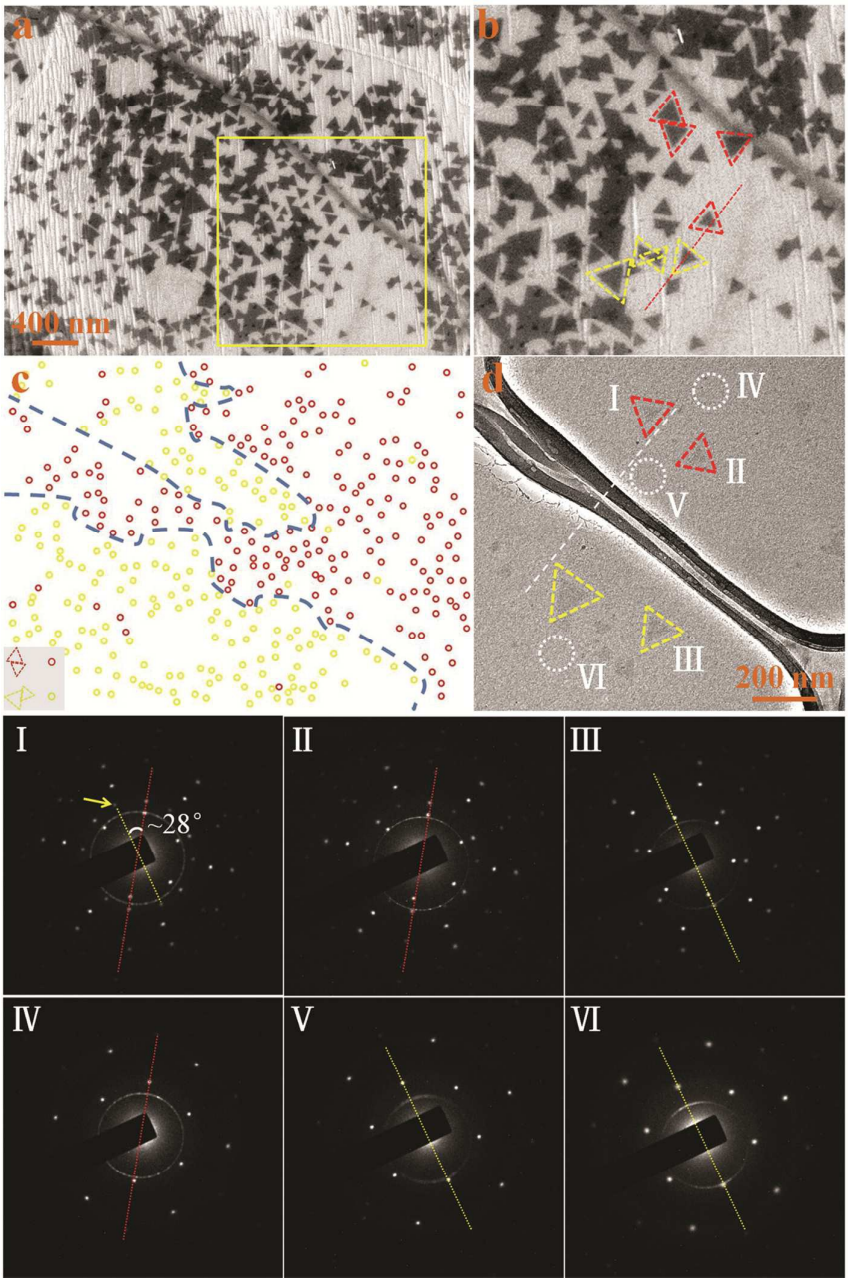

Fig. 4 (a) SEM image of an area consists of two orientations of MoS_2 crystallites on Gr/Pt. (b) The zoomed-in SEM image of the framed area in (a). The two different orientations of MoS_2 which rotate by a relative angle of about 28° are marked with yellow and red dashed triangles, respectively. (c) The distribution of MoS_2 triangles with different orientations in (a). The boundaries of different orientations are discernible with blue dashed lines. (d) TEM image of MoS_2 crystallites with two different orientations. The SAED patterns of selected areas are respectively shown below with corresponding numbers.

the high-magnification TEM image of MoS_2 in Fig. 3b, which exhibits a lattice constant of about 0.315 nm estimated from the TEM image, consistent with that of MoS_2 (a = 0.312 nm). The selected-area electron diffraction (SAED) was measured to determine the relative orientation of the MoS_2 and Gr from the area in Fig. 3b. In the SAED pattern that illustrated in the upper right corner of Fig. 3c, two sets of hexagonal diffraction patterns that originated from MoS_2 to Gr can be clearly seen, indicating that both MoS_2 and Gr have high crystallinity. Due to the larger lattice constant of MoS_2 (a = 0.312nm) compared to that of Gr (a = 0.246nm), the brighter diffraction spots located closer to the center beam highlighted by a hexagon are the first order of MoS_2. The dimmer ones are believed from Gr. These two sets of diffraction patterns have an identical orientation, indicating the good alignment of MoS_2 with Gr.

However, in some areas (typically shown in Fig. 4a), we observe that some MoS_2 triangles rotate by a relative angle of about 28° ± 2°, as marked with red and yellow dashed triangles in Fig. 4b (the enlarged area selected in Fig. 4a). In order to analysis the distribution of these two types of MoS_2 triangles, we use red and yellow circle dots to represent them, as illustrated in Fig. 4c. Obviously, the two types are located in their respective areas with a few exceptions that possibly due to the existing defects in CVD-Gr. Considering the Gr grown on Pt is a polycrystalline film, we suppose that the reason why there is not a uniform orientation for MoS_2 on Gr/Pt may lies in the different domain orientations exist in the Gr. It has been demonstrated that the continuous Gr boundaries composed by alternating pentagons and heptagons is the primary cause of a constant crystal orientation of about 27° relatively tilted between the two grains, [33, 34] which is similar to our observation of the included angle between the two types of triangular MoS_2. Since the structures of MoS_2 with different orientations on Gr can be determined by TEM accurately, it is easy for us to get further demonstration. The TEM image containing both types of MoS_2 triangles is shown in Fig. 4d. The SAED patterns of three MoS_2 domains (labelled as I, II, and III, where I and II are the same type triangles with opposing directions) as well as the adjacent areas of bare Gr (labelled as IV, V, and VI) are shown below, respectively. Comparing with the SAED patterns of I to III, we find that the diffraction patterns of MoS_2 are always corresponding to that of Gr in spite of the different orientations they appear, as indicated by the red and yellow dashed lines in the SAED patterns. Meanwhile, by comparing the SAED patterns of the adjacent Gr areas (IV to VI) with that of MoS_2/Gr (I to III), we observe that the SAED patterns of Gr in I, II and IV are completely coincident, while the SAED pattern of Gr in III is well consistent with those in V and VI. This illustrates that the two types of MoS_2 triangles are grown on two different Gr domains. Additionally, in the images of SAED patterns I and II, there is another relative darker set of diffraction pattern (one spot of this set is indicated by a yellow arrow). We owe it to the adjacent Gr domain, as inferred by their pattern characteristics which show the same hexagonal features as the SAED patterns V and VI. The included angle of these two sets of diffraction pattern from Gr is found to be equal to that of the two-type

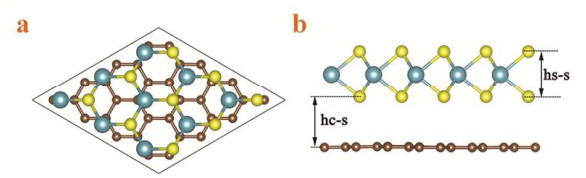

Fig.5 Top and side views of MoS_2/Gr heterostructure. C, Mo, and S atoms are represented by brown, purple, and yellow balls, respectively.

orientations of MoS_2. Further measurements on the distance of the diffraction points of the two sets Gr pattern in a same SAED image indicate that the lattice of MoS_2-covered Gr is compressed, comparing with that of the adjacent bare Gr. Based on the analysis on more than ten SAED patterns of MoS_2/Gr, the compression ratio of Gr lattice is estimated to be 0.705% ± 0.253%. Our investigations of direct synthesis of MoS_2 on polycrystalline CVD-Gr on Pt clearly reveal the strict epitaxial growth of MoS_2 on Gr, and offer us an easy approach to find out the orientation of Gr domains without transferring. Such a strict epitaxial mechanism is different from the growth of MoS_2 on sapphire or GaSe and WSe_2 domains on Gr that either shows multiple epitaxial orientations [35, 36] or larger interlayer rotation with respect to the underlying Gr, [37] indicating that there may be strong correlation in the heterostructure of MoS_2 and Gr.

To understand the interaction between MoS_2 layer and its Gr substrate as well as the structural and electronic properties of MoS_2/Gr heterostructure, first-principles calculations of the MoS_2/Gr heterostructure have been carried out. Based on the experimental founding as discussed above, we employed a supercell consisting of 32 C atoms (4×4 unit cells of Gr), 9 Mo atoms and 18 S atoms (3×3 unit cells of MoS_2 monolayer) for the MoS_2/Gr heterostructure calculation, as shown in Fig. 5. Our calculated lattice constant of an isolated Gr is 0.245 nm ($a_{Gr} = \sqrt{3}d_{C-C}$, which d_{C-C} is the carbon−carbon bond length), while the optimized lattice constant of a monolayer MoS_2 is 0.312 nm. Thus, the lattice mismatch in the supercell initially for MoS_2/Gr is less than 4.5%. After relaxation, the lattice constant of MoS_2 layer is expanded by 3.2%, while the lattice constant of Gr sheet is compressed by 1.4%, as shown in Table 1. The compressed lattice of Gr layer agrees well with our experimental results. The calculated Mo-S bond lengths of 0.240 nm in the MoS_2/Gr are larger than that of the isolated monolayer MoS_2 (0.238 nm), whereas the C-C bond lengths of 0.139 nm in the MoS_2/Gr are shorter than that of the free-standing Gr (0.141 nm). The interlayer distance between Gr and adjacent S atomic layer (marked with h_{C-S}) is found to be 0.333 nm, which is larger than the sum of the covalent radius of C and S atoms (0.181 nm). This suggests that van der Waals interactions could be the primary interactions between two sheets in the MoS_2/Gr heterostructure. To discuss the relative stabilities of the MoS_2/Gr heterostructure, the binding energy between the stacking sheets in the bilayer is defined as $E_b = [(E_{MoS_2} + E_{Gr}) - E_{supercell}] / N$, where $E_{supercell}$ is the total energy

Table 1. Geometries and Binding Energies of the MoS_2/Gr heterostructure, isolated Gr and free-standing monolayer MoS_2, including the lattice constant (a), C-C bond length (d_{c-c}), Mo-S bond length (d_{Mo-S}), MoS_2 sheet thickness (h_{S-S}), interlayer distance between Gr and nearest S atom layers (h_{C-S}) and binding energy per C atom (E_b).

System	a (nm)	d_{c-c} (nm)	d_{Mo-S} (nm)	h_{S-S} (nm)	h_{C-S} (nm)	E_b (meV/C atom)
MoS_2/Gr	0.966	0.139	0.240	0.305	0.333	22
4×4 Gr	0.980	0.141				
3×3 MoS_2	0.936		0.238	0.311		

per supercell and E_{MoS_2} and E_{Gr} are the total energies of the 3×3 MoS_2 monolayer and 4×4 Gr sheet, respectively. *N* is the number of C atoms in the supercell, E_b is the interlayer binding energy per C atom. The adsorption energy of MoS_2/Gr heterostructure is positive (22 meV/C atom), which indicates that the chemical absorption effect of the MoS_2 monolayer on Gr layer cannot be ignored.

In order to make a further discussion on the electronic structures of MoS_2/Gr heterostructure, we also calculated its band structure and the density of states (shown in Fig. 6). Our results reveal that the MoS_2/Gr exhibits metallic electronic properties (shown in Fig. 6a). As well known, the Dirac point in the isolated Gr is at the Fermi level; however, the Fermi level of MoS_2/Gr heterostructure is shifted down to below the Dirac point of Gr layer. Since the electronic states around Fermi level at K-point are all contributed from Gr layer (shown in Fig. 6b), the shift of Fermi level suggests that the Gr sheet lose electrons during the formation of MoS_2/Gr heterostructure, which is consistent with our observation of the up-shift of Gr Raman 2D band. To further explore the charge transfer between the stacking layers in the MoS_2/Gr heterostructure, the contour plots of the charge density difference (Δρ) of the plane perpendicular to the Gr and MoS_2 layers (highlighted in blue shades) is presented in Fig. 6c. The charge density difference (Δρ) is defined as $\Delta\rho(\vec{r}) = \rho(\vec{r}) - (\rho_{slab}(Gr) + \rho_{slab}(MoS_2))$, where $\rho(\vec{r})$, $\rho_{slab}(Gr)$ and $\rho_{slab}(MoS_2)$ are charge densities of the MoS_2/Gr heterostructure, the Gr and the MoS_2 sheets, respectively. As shown in Fig. 6c, we can clearly see the charge transferred from the Gr layer to the MoS2 layer. Such charge transfer is the primary cause of the metallicity of MoS_2/Gr heterostructure.

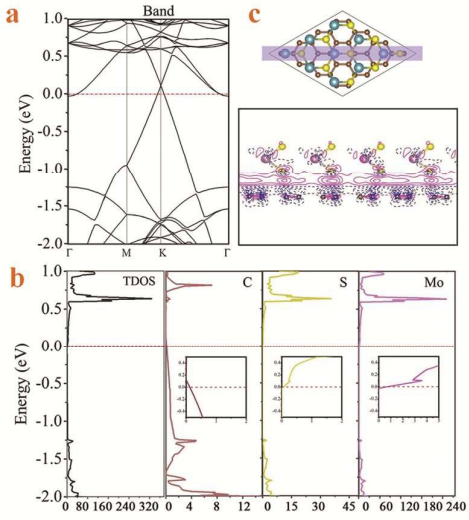

Fig. 6 (a) Band structure, (b) density of states and (c) charge density differences on a plane perpendicular to the Gr and MoS_2 layers, passing through C-C and Mo-S atoms for the MoS_2/Gr heterostructure. Detailed densities of states near the Fermi level are inserted. Solid pink and dashed blue lines correspond to Δρ>0 and Δρ<0, respectively. Red dashed line represents the Fermi level.

The existent of interlayer coupling and considerable strain in MoS_2/Gr heterostructure can also be directly perceived through the discovery of plentiful cracks in the successfully synthesized large scale few-layer MoS_2 (average separation between $E_{2g}{}^1$ and A_{1g} is about 23 cm^{-1}) on Gr/Pt, as shown in Fig. 7a. In our attempt to grow large scale MoS_2 on Gr, we find that there are many cracks appeared in the as-grown film, and the width of such cracks can be extended to several hundred nanometers. The cracks often show like zigzag, the flex angles are either 120° or 60°. Since such a phenomenon has not been occurred in our annealing of Gr on Pt at 1000°C, we believe that the strong interlayer coupling and the big difference of strain in MoS_2 and Gr may contribute to cracks, as discussed above. And also because of the positive thermal expansion coefficients of MoS_2, it is easy to conclude that such cracks are only in the MoS_2 layer. Comparing with the collected Raman spectrum of MoS_2 crystallites on Gr/Pt, both G and 2D bands of the Gr that covered with large scale MoS_2 are downshifted and practically turning back to their previous position of bare Gr, as shown in Fig. 7b. This indicates that such cracks can counteract the strain in MoS_2 and Gr effectively, which also gives the direct evidence that the effective interlayer coupling with the MoS_2 domains and the local strain induced during the MBE

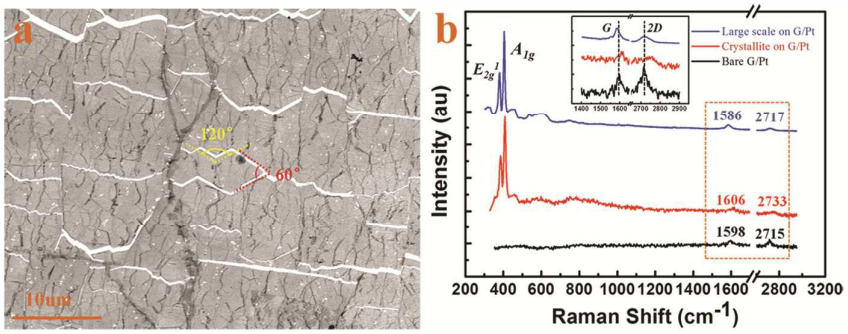

Fig. 7 (a) Large-area few-layer MoS_2 grown on Gr/Pt with many cracks induced by interlayer strain. The flex angles of the cracks are either 120° or 60°. (b) Raman spectra of the bare Gr/Pt (black), MoS_2 crystallites (red) and large scale MoS_2 (blue) on Gr/Pt. The details of G and 2D bands of Gr are illustrated in the upper and middle part of (b).

growth process both contribute to the observed upshift of the Raman G and 2D bands of Gr.

Conclusions

In this study, the MoS_2/Gr heterostructure was successfully synthesized by direct epitaxial growth methods, which enables us to investigate the growth mechanisms and interlaminar interaction of the heterostructure without sample handling and transfer. The subsequent SEM and TEM characterizations clearly revealed the growth of MoS_2 on Gr followed the strict epitaxial mechanism. The interlayer coupling and strain effect in the heterostructure were responsible for the observed upshift of the Raman G and 2D bands of Gr, which was further proved by the presence of zigzag cracks in the epitaxial large-scale MoS_2 layers on Gr. Based on first-principles calculations, we had demonstrated the structure characteristics of MoS_2/Gr heterostructure, and revealed its electronic properties which exhibited metallicity due to the charge transfer from Gr to MoS_2. The synthesis of high quality MoS_2/Gr films and the investigations on their properties offer us inspiration for the application of such heterostructures in electronic and photonic devices.

Acknowledgements

We appreciate the support from by the National Natural Science Foundation of China (Grant Nos. 91123009 and 11574257), the Natural Science Foundation of Fujian Province of China (Grant Nos. 2012J06002 and 2015J01030), and the Fundamental Research Funds for Central Universities (Grant No. 20720150033).

Notes and references

1 Q. Wang, K. Kalantar-Zadeh, A. Kis, J. Coleman and M. Strano, *Nat. Nanotechnol.*, 2012, **7**, 699.
2 M. Chhowalla, H. Shin, G. Eda, L. Li, K. Loh and H. Zhang, *Nat. Chem.*, 2013, **5**, 263.
3 K. S. Novoselov, D. Jiang, F. Schedin, T. Booth, V. Khotkevich, S. Morozov and A. Geim, *Proc. Natl. Acad. Sci. USA*, 2005, **102**, 10451.
4 H. Liu, A. Neal, Z. Zhu, Z. Luo, X. Xu, D. Tománek and P. Ye, *ACS Nano*, 2014, **8**, 4033.
5 C. Sabina, R. Weatherup, B. Bayer, B. Brennan, S. Spencer, K. Mingard, A. Cabrero-Vilatela, C. Baehtz, A. Pollard and S. Hofmann, *Nano Lett.*, 2015, **15**, 1867.
6 H. Lim, S. Yoon, G. Kim, A. Jang and H. Shin, *Chem. Mater.*, 2014, **26**, 4891.
7 G. Lee, Y. Yu, X. Cui, N. Petrone, C. Lee, M. Choi, D. Lee, C. Lee, W. Yoo and K. Watanabe, *ACS Nano*, 2013, **7**, 7931.
8 X.D. Li, S. Yu, S.Q. Wu, Y.H. Wen, S. Zhou and Z.Z. Zhu, *J. Phys. Chem. C*, 2013, **117**, 15347; X.D. Li, S.Q. Wu, S. Zhou and Z.Z. Zhu, *Nanoscale Res. Lett.* 2014, **9**, 110; S. Yu, X.D. Li, S.Q. Wu, Y.H. Wen, S. Zhou and Z.Z. Zhu, *Mater. Res. Bull.*, 2014, **50**, 268; X.D. Li, S.Q. Wu and Z.Z. Zhu, *J. Mater. Chem. C*, 2015, **3**, 9403.
9 W. Yu, Y. Liu, H. Zhou, A. Yin, Zheng Li, Y. Huang and X. Duan, *Nat. Nanotechnol.*, 2013, **8**, 952.
10 J. Yu, Z. Li, H. Zhou, Y. Chen, Y. Wang, Y. Huang and X. Duan, *Nat. Mater.*, 2013, **12**, 246.
11 S. Bertolazzi, D. Krasnozhon and A. Kis, *ACS Nano*, 2013, **7**, 3246.
12 A. Ebnonnasir, B. Narayanan, S. Kodambaka and C. Ciobanu, *Appl. Phys. Lett.*, 2014, **105**, 031603.
13 E. O'Farrell, A. Avsar, J. Tan, G. Eda and B. Özyilmaz, *Nano Lett.*, 2015, **15**, 5682.
14 A. Azizi, S. Eichfeld, G. Geschwind, K. Zhang, B. Jiang, D. Mukherjee, L. Hossain, A. Piasecki, B. Kabius and J. Robinson, *ACS Nano*, 2015, **9**, 4882.
15 K. McCreary, A. Hanbicki, J. Robinson, E. Cobas, J. Culbertson, A. Friedman, G. Jernigan and B. Jonker, *Adv. Funct. Mater.*, 2014, **41**, 6449.
16 H. Ago, H. Endo, P. Solís-Fernández, R. Takizawa, Y. Ohta, Y. Fujita, K. Yamamoto and M. Tsuji, *ACS Appl. Mater. Interfaces*, 2015, **7**, 5265.
17 Y. Lin, N. Lu, N. Perea-Lopez, J. Li, Z. Lin, X. Peng, C. Lee, C. Sun, L. Calderin, P. Browning, M. Terrones and J. Robinson, *ACS Nano*, 2014, **8**, 3715.
18 Y. Shi, W. Zhou, A. Lu, W. Fang, Y. Lee, A. Hsu, S. Kim, K. Kim, H. Yang and L. Li, *Nano Lett.*, 2012, **12**, 2784.
19 G. Kresse and D. Joubert, *Phys. Rev. B*, 1999, **59**, 1758.
20 G. Kresse and J. Furthmüller, *Comput. Mater. Sci.*, 1996, **6**, 15.
21 G. Kresse and J. Furthmüller, *Phys. Rev. B*, 1996, **54**, 11169.
22 D. Ceperley and B. Alder, *Phys. Rev. Lett.*, 1980, **45**, 566.
23 J. Perdew and A. Zunger, *Phys. Rev. B*, 1981, **23**, 5048.

24 T. Gao, S. Xie, Y. Gao, M. Liu, Y. Chen, Y. Zhang and Z. Liu, *ACS Nano*, 2011, **5**, 9194.
25 J. Gao, K. Sagisaka, M. Kitahara, M. Xu, S. Miyamoto and D. Fujita, *Nanotechnology*, 2012, **23**, 055704.
26 J.Sun, Y. Nam, N. Lindvall, M. Cole, K. Teo, Y. Park and A. Yurgens, *Appl. Phys. Lett.*, 2014, **104**, 152107.
27 X. Li, W. Cai, J. An, S. Kim, J. Nah, D. Yang, R. Piner, A. Velamakanni, I. Jung and E. Tutuc, *Science*, 2009, **324**, 1312.
28 K. Zhou, F. Withers, Y. Cao, S. Hu, G. Yu and C. Casiraghi, *ACS Nano*, 2014, **8**, 9914.
29 S. El-Mahalawy and B. Evans, *J. Appl. Crystallogr.*, 1976, **9**, 403.
30 D.Yoon, Y. Son and H. Cheong, *Nano Lett.*, 2011, **11**, 3227.
31 Y. Zhan, Z. Liu, S. Najmaei, P. M. Ajayan and J. Lou, *small*, 2012, **8**, 966.
32 Y. Wang , C. Cong , C. Qiu and T. Yu, *small*, 2013, **9**, 2857.
33 W. Guo, B. Wu, Y. Li, L. Wang, J. Chen, B. Chen, Z. Zhang, L. Peng, S. Wang and Y. Liu, *ACS Nano*, 2015, **9**, 5792.
34 O.Yazyev and S. Louie, *Phys. Rev. B*, 2010, **81**, 195420.
35 D. Dumcenco, D. Ovchinnikov, K. Marinov, P. Lazić, M. Gibertini, N. Marzari, O. Sanchez, Y. Kung, D. Krasnozhon and M. Chen, *ACS Nano*, 2015, **9** , 4611.
36 B. Wang, S. M. Eichfield, D. Wang, J. A. Robinson and M. A. Haque, *Nanoscale*, 2015, **7**, 14489.
37 S. Xu, Y. Han, X. Chen, Z. Wu, L. Wang, T. Han, W. Ye, H. Lu, G. Long and Y. Wu, *ACS Nano*, 2015, **9**, 8078.

TOC

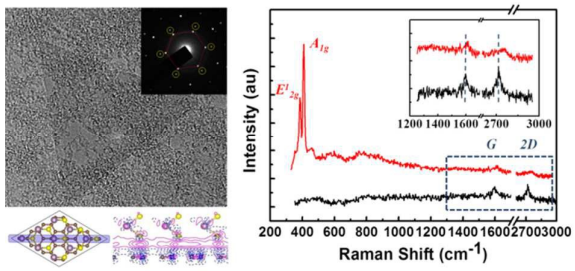

The triangular monolayer MoS_2 directly synthesized on CVD-G on Pt reveals a strong correlation between each other.